Advanced Materials Technologies

ADVANCED MATERIALS TECHNOLOGIES
www.advmattechnol.com

RESEARCH ARTICLE OPEN ACCESS

3D Printed PEDOT:PSS-Based Lattice Pressure Sensors With Tunable Electromechanical Response

Ozan Karakaya[1,2] | Naroa Lopez-Larrea[3] | Ali Veysel Tunc[1,2] | Mikel Rincon-Iglesias[1,2,4] | Karin J. Chen[5] | Katja Nau[5] | Senentxu Lanceros-Mendez[4,6] | David Mecerreyes[3,6] | Miryam Criado-Gonzalez[3,7] | Gerardo Hernandez-Sosa[1,2,5,8]

[1]Light Technology Institute, Karlsruhe Institute of Technology (KIT), Karlsruhe, Germany | [2]InnovationLab GmbH, Heidelberg, Germany | [3]POLYMAT, University of the Basque Country UPV/EHU, San Sebastián, Spain | [4]BCMaterials, Basque Center for Materials, Applications and Nanostructures, UPV/EHU Science Park, Leioa, Spain | [5]Institute for Automation and Applied Informatics, Karlsruhe Institute of Technology (KIT), Eggenstein-Leopoldshafen, Germany | [6]Ikerbasque, Basque Foundation for Science, Bilbao, Spain | [7]Institute of Polymer Science and Technology (ICTP-CSIC), Madrid, Spain | [8]Institute of Microstructure Technology, Karlsruhe Institute of Technology (KIT), Eggenstein-Leopoldshafen, Germany

Correspondence: Gerardo Hernandez-Sosa (gerardo.sosa@kit.edu)

Received: 30 September 2025 | **Revised:** 11 February 2026 | **Accepted:** 25 February 2026

Keywords: 3D printed electronics | additive manufacturing | metastructure architecture design | tactile sensing | tunable pressure sensors

ABSTRACT

3D printed pressure sensors show broad potential, owing to their tunable mechanical and electrical properties. Meta-structures are ideal candidates for such sensors, thanks to their lightweight nature and customizable mechanical behavior. In this study, we present 3D-architected pressure sensors fabricated in a single step via digital light processing (DLP) 3D printing of a poly(3,4-ethylenedioxythiophene): polystyrene sulfonate (PEDOT:PSS)-based photoresin. The electromechanical characteristics of an X-Cell lattice are optimized by varying parameters such as relative density and lattice count to enhance manufacturability, sensitivity, and pressure range. The X-cell lattice with 40% relative density and 64-unit cells exhibits a sensitivity of 17.7 ± 5.8 kPa^{-1} in the 0–15 kPa range, and 9.11 ± 4.19 kPa^{-1} across a broader range of 15–120 kPa, demonstrating its suitability for both high-sensitivity and wide-range pressure sensing applications. Optimization is further extended to fabricate Gyroid and Schwarz D lattices showing initial sensitivities of 40.03 ± 0.64 and 7.4 ± 0.7 kPa^{-1}, respectively. A proof-of-concept tactile sensor is developed by integrating multiple lattice designs into a single active layer. Requiring only two electrodes, this sensor leverages distinct electromechanical responses to localize pressure, eliminating complex arrays and enabling efficient development of next-generation tactile sensors.

1 | Introduction

With the rapid advancement of the Internet of Things (IoT), the demand for sensors that enable seamless interaction between humans and electronic systems has grown significantly [1]. Among these, flexible pressure sensors have attracted considerable attention due to their potential applications in soft robotics [2, 3], wearable health monitoring [4, 5], and electronic skin technologies [6–8]. Based on their sensing mechanisms, pressure sensors are typically categorized into piezoelectric, piezoresistive, and capacitive types. Among them, piezoresistive sensors are widely adopted due to their high sensitivity, simple signal processing, and broad material compatibility, and are used in soft sensor applications such as smart grippers and electronic switches. [9–16]

In parallel with advances in new materials and processing techniques, 3D additive manufacturing of pressure sensors has attracted considerable attention for enabling spatially resolved sensing, improved device integration, and tunable mechanical and electrical properties [17–19]. 3D-printed metamaterials, with their architected structures, offer a powerful design space for tailoring pressure sensor performance [20–22]. Previous studies have explored 3D extrusion printing methods such as fused deposition modeling (FDM) and direct ink writing (DIW) to create metamaterial-based pressure sensors [23–26]. Massroni et al. demonstrated the fabrication of pressure sensors by printing various geometries with different infill patterns using a conductive polyurethane-based filament [27]. Their approach enabled tunable sensor performance, achieving a maximum sensitivity of $-6.3\ kPa^{-1}$. Similarly, Xiao et al. used DIW to fabricate graphene nanoplatelet/PDMS-based sensors with a sensitivity of $0.0602\ kPa^{-1}$ over a 0–350 kPa range [24]. However, extrusion-based printing is primarily intended for large-scale structures and faces significant challenges when fabricating the intricate, support-dependent geometries typical of metamaterial designs.

Vat photopolymerization techniques, such as stereolithography (SLA) and Digital Light Processing (DLP), offer superior resolution for printing complex lattice structures. However, the bulk printing of conductive materials remains a significant challenge due to the limited availability of functional photoresins. Conductive materials, in particular, tend to absorb UV–vis light, leading to scattering and reduced printing efficiency for most light-based printing technologies [28]. To address this limitation, post-processing techniques such as dip-coating have been explored. Zhao et al. demonstrated a metamaterial-based pressure sensor in which a 3D-printed insulating polyacrylate structure underwent a two-step surface coating process with Al_2O_3 followed by ZnO [20]. Their study investigated the sensing performance of various meta-structured designs, achieving a detection range of 0–15 MPa. Yin et al. used a similar approach with CNT-based coatings, achieving a sensitivity of $1.02\ kPa^{-1}$ over a 0.7 Pa–160 kPa range [19]. However, these methods often face challenges such as non-uniform coatings, cracking during deformation, and time-consuming fabrication processes.

Direct light-based printing of conductive or semiconductive materials remains relatively underexplored [29]. In one seminal example, Xia et al. reported a strain-stable, flexible pressure sensor featuring complex geometries, fabricated using a composite photoresist that combined a photocurable resin and multi-walled carbon nanotubes as a conductive filler [30]. The prepared slurry was processed via DLP printing, and the resulting sensor exhibited a minimal resistance variation of 0.76% and a pressure sensitivity change of only 0.22% under 20% applied strain. Xiao et al. demonstrated a fully DLP-printed sensor with a woodpile structure and a sensitivity of $15.04\ MMPa^{-1}$ under 64.44 kPa [31]. However, carbon nanotubes and metallic fillers pose challenges such as cytotoxicity, aggregation, and limited mechanical tunability. Alternatively, poly(3,4-ethylenedioxythiophene): polystyrene sulfonate (PEDOT:PSS), a conductive and biocompatible polymer widely used in optoelectronics and bioelectronics research, has also been employed as a piezoresistive material due to its inherent π-conjugated system and favorable electronic properties [10, 32, 33]. Despite its advantages, direct vat photopolymerization of PEDOT:PSS result challenging due to its high optical absorption, which limits light penetration during polymerization. However, recent studies have demonstrated successful 3D light-based printing of bulk PEDOT:PSS, overcoming this limitation by adjusting the photopolymerization kinetics and the used light wavelength [34–36]. The integration of mechanically tunable metamaterial designs with conductive, piezoresistive PEDOT:PSS homogeneously distributed throughout the structure holds significant potential for developing flexible sensors with both mechanical and electronic tunability for more versatile bioelectronic applications.

In this study, we demonstrate the single-step fabrication of architected piezoresistive pressure sensors with electromechanically tunable properties, achieved by DLP 3D printing. These sensors were fabricated using a recently developed PEDOT:PSS-based conductive acrylic photoresin, enabling the direct printing of architected metamaterial structures with a lateral resolution of 27 µm and a vertical resolution of 50 µm. We conducted a comparative analysis of three metastructure designs, focusing on relative density, unit cell count, and lattice geometry, which are key parameters that influence sensor sensitivity and pressure range. To systematically investigate the influence of structural parameters on sensor performance, we first fabricated X-cell lattice structures with 64-unit cells and varied their relative densities at 20%, 30%, and 40%. This allowed us to evaluate the effect of infill level on electromechanical behavior. Next, we examined the effect of unit cell count by fabricating X-cell structures with 27, 64, and 125-unit cells at a fixed relative density. Additionally, Gyroid and Schwarz D structures were fabricated using optimized parameters derived from earlier design stages. These three lattice topologies were selected on the basis of their suitability for additive manufacturing and their markedly tunable, distinct electromechanical responses [16, 37–42]. Finally, we demonstrate a proof-of-concept sensor integrating three distinct lattice geometries, each exhibiting unique pressure response characteristics. This kind of proof-of-concept sensor eliminates the need for traditional complex electrode arrays, paving the way for the development of next-generation tactile sensors.

2 | Results and Discussion

2.1 | Vat 3D Printable Conductive PEDOT:PSS Structures

Figure 1a presents the single-step fabrication process of the piezoresistive pressure sensor beginning with the formulation of the conductive PEDOT:PSS photoresin and the subsequent layer-by-layer fabrication via vat photopolymerization using a DLP 3D printer. In vat photopolymerization-based printing, the polymer network formation occurs through a light-mediated free radical polymerization mechanism.

The photoinitiator within the photoresin generates free radicals upon exposure to light, which then react with acrylate-based monomers to initiate the polymer growth. The final structure is a polyethylene glycol acrylic crosslinked network where PEDOT:PSS is trapped. The photo-DSC thermogram of PEDOT:PSS based photoresin (Figure 1b) shows the release of exothermic heat following a 1-s pulse of UV light (320–390 nm) at an intensity of $5\ mW\ cm^{-2}$. This exothermic heat generation during the light-curing process confirmed that the polymerization reaction occurred in this wavelength range. Figure 1c shows examples of different lattice structures that were DLP 3D printed with an identical number of unit cells and varying the overall dimensions, which ranged from 5 mm to 5 cm in length, by keeping the aspect ratio and achieving feature sizes as small as

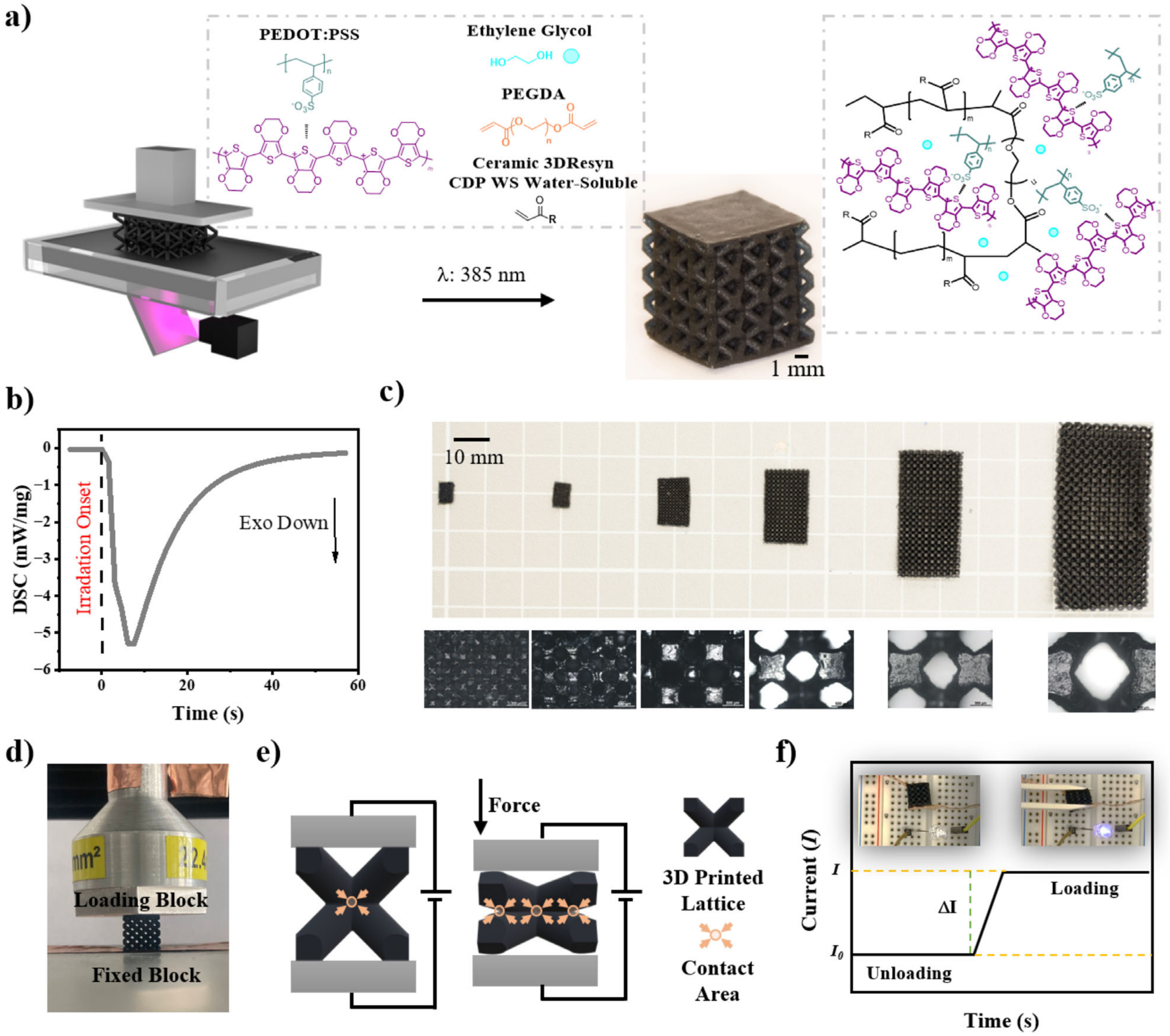

FIGURE 1 | (a) Vat photopolymerization printing process of 3D lattice-based pressure sensors and corresponding ink formulation (inset). (b) The photo-Differential Scanning Calorimetry (photo-DSC) thermogram of the PEDOT:PSS based photoresin. (c) Pictures and corresponding microscope images of X-Cell lattice structures with different dimensions. (d) Photograph of the in situ electromechanical measuring setup. (e) Schematic illustration of the working mechanism of 3D lattice-based pressure sensors. (f) Demonstration of the electrical response of the lattices under the application of external pressure.

40 µm. The printed structures were composed of 50 µm slices corresponding to a 2-s exposure time ($\lambda = 385$ nm) during the DLP process (Figure S1). The developed printing process demonstrates the capability of the single-step DLP-based additive manufacturing process to produce fine-featured, conductive PEDOT:PSS structures with high geometric fidelity. Throughout this work, the electromechanical behavior of the 3D-printed lattice structures was evaluated by simultaneously measuring lattice displacement and electrical current between the loading and fixed blocks, as illustrated in Figure 1d. The working principle of the 3D-printed PEDOT:PSS piezoresistive sensors is schematically illustrated in Figure 1e. In the initial state, PEDOT:PSS chains have minimal contact, resulting in low electrical conductivity. When pressure is applied, the lattice walls come into closer contact, forming additional conductive pathways and increasing sensitivity. As deformation progresses, more contact points are established, further enhancing conductance and reducing overall resistance [43, 44]. To visualize this mechanism, a schematic including an electrical current–time plot and a simplified circuit diagram was created and shown in Figure 1f, where the conductive lattice is connected to a battery and an LED. In the compressed state, the increased contact between lattice walls creates sufficient conductive pathways to allow enough current to illuminate the LED.

2.2 | Tunable Electromechanical Properties of 3D Printed Conductive Structures

Figure 2a presents the photographs and corresponding microscope images of X-Cell-based structures fabricated with relative densities of 20%, 30%, and 40%. The perceived color difference on

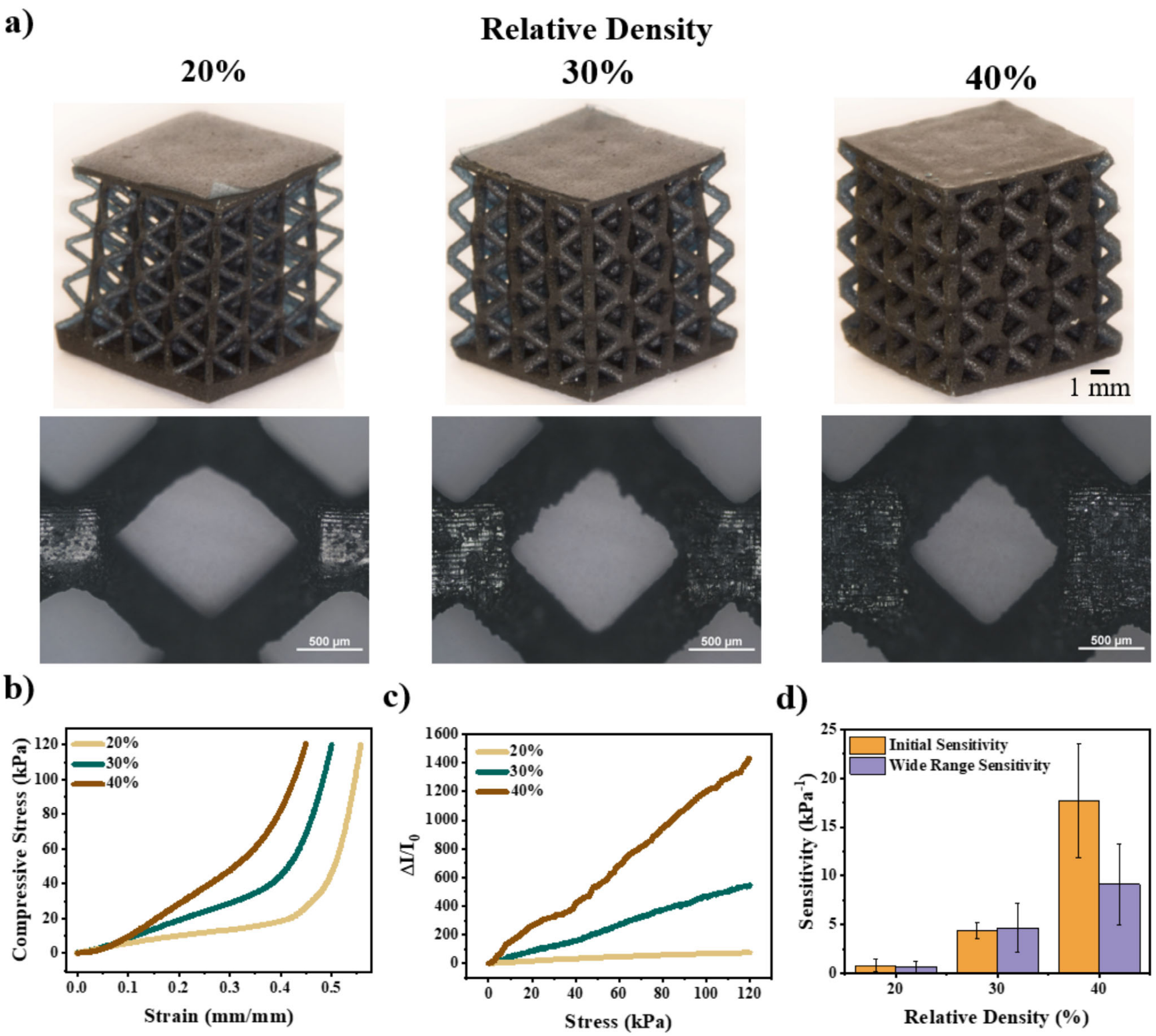

FIGURE 2 | (a) Photographs and corresponding microscope images of the 3D-printed X-Cell lattices (64 unit cells) with relative densities of 20%, 30%, and 40%, respectively. (b) Compressive stress-strain curves of the 3D printed lattices with different relative densities. (c) Conductivity changes vs. compressive stress for the 3D printed lattices with different relative densities. (d) Mean sensitivities of the 3D printed lattices in different pressure ranges.

the top of the printed cubes corresponds to the reflection of the illumination source, not to a change in the material composition. Each lattice contains 64-unit cells and is embedded between two protective square layers, each of them with an area of 1 cm^2 and a height of 0.5 mm, to ensure structural integrity during mechanical testing. All printed structures exhibited a high resolution, but as the relative density decreased, a noticeable reduction in strut thickness was observed, resulting in a more open and compliant lattice architecture. Relative densities below 20% led to mechanical instability and the collapse of the structures without any applied pressure. Figure 2b shows the compressive stress–strain curves of the printed lattices, highlighting their mechanical responses across varying relative densities. All samples were compressed up to 120 kPa. As expected, Young's modulus (E) increases with the density of the samples from 36 $\pm$ 10 kPa for lattices with 20% relative density to 180 $\pm$ 10 kPa for the ones at 40%. Conversely, yield strength decreased with increasing relative density. The elastic region of the lattice with 20% relative density was extended up to 43% strain. In contrast, lattices with 30% and 40% relative densities exhibited a reduced elastic region up to 35% and 28% strain, respectively. This behavior is attributed to the increase in strut thickness at higher lattice densities, which increases the resistance to deformation, reducing the displacement upon compression forces.

The electromechanical performance was evaluated by measuring the change in electrical current, $\Delta I/I_0$, as a function of the applied pressure for each lattice (Figure 2c). ΔI represents the difference between the initial current I_0, in the absence of external pressure, and the current I, measured under compressive stress. It can be observed that increasing the relative density or infill level resulted in greater relative changes in the conducted current, indicating a direct correlation between the increased amount of material deposited and the sensor's sensitivity. The sensitivity, S, of a

TABLE 1 | Sensitivities[a] and corresponding pressure ranges of lattices with relative densities from 20% to 40% with 64-unit cells.

Lattice		Initial range		Wide range	
Geometry	Relative density (%)	Pressure range (kPa)	Sensitivity (kPa^{-1})	Pressure range (kPa)	Sensitivity (kPa^{-1})
X-Cell	20	0–40	0.80 ± 0.69	40–120	0.64 ± 0.60
X-Cell	30	0–20	4.41 ± 0.84	20–120	4.67 ± 2.49
X-Cell	40	0–15	17.7 ± 5.8	15–120	9.11 ± 4.19
Schwarz D	40	0–20	7.4 ± 0.7	20–120	2.06 ± 1.32
Gyroid	40	0–10	40.03 ± 0.64	10–120	1.63 ± 1.16

[a] All values of sensitivity from this work are reported as mean and standard deviation with $n \geq 3$.

piezoresistive sensor is defined as $S = (\delta I/I_0)/\delta P$, where δP denotes the change in applied pressure. From Figure 2c, we identified two linear sensitivity regimes for each of the relative lattice densities: the initial region, representing early-stage pressure response, and the wide-range sensitivity region, covering up to the highest applied pressure. The presence of different pressure regimes can be attributed to the interplay between material properties and structural design, which results in distinct conduction mechanisms occurring at various pressure levels. At low pressures, sensors demonstrated high sensitivity due to the easy deformation and the rapid extension of the contact area. In contrast, the relatively lower sensitivity observed at higher pressures can be attributed to the further densification of the microstructures [45, 46]. The pressure regimes were defined using a linear fit over the broadest range of applied pressures below 40 kPa, maintaining a linearity, with a regression coefficient R^2 exceeding 0.96. The corresponding sensitivities were calculated based on this linear fit, as shown in Figure S2. Table 1 summarizes the extent of the regions and the sensitivity corresponding to each relative lattice density for X-Cell, as well as for the different 3D printed structures at a relative density of 40%.

The lattice with 40% relative density exhibited the highest mean sensitivity, reaching 17.7 ± 5.8 kPa^{-1} in the initial region and 9.11 ± 4.19 kPa^{-1} across the wide range. Figure 2d illustrates the relationship between relative density and sensitivity, showing that a change from 20% to 40% in lattice relative density resulted in approximately a 22- and 14-fold enhancement in initial and wide range sensitivities, respectively. This tendency is attributed to the higher PEDOT:PSS content in denser lattices, which promotes the formation of additional conductive pathways under compression, thereby increasing the current flow. Notably, the increase in sensitivity led to a narrower linear detection range in the initial sensitivity region, indicating a trade-off between the sensitivity and linear pressure range of the sensors [47].

In addition to the relative density, the number of unit cells within the lattice structure is another critical parameter influencing stress distribution and mechanical performance. Then, we focused on the most sensitive lattices, with 30% and 40% relative densities, to investigate the effect of the unit cell count on the electromechanical properties of the sensors.

Figure 3a shows optical microscopy images of the investigated X-Cell lattice structures comprising 27, 64, and 125-unit cells. All 3D printed structures presented a high resolution. As the unit cell count increased, a noticeable reduction in strut thickness was observed, resulting in a more porous lattice architecture. The corresponding Young's moduli of the structures are presented in Figure 3b. An increase in the number of unit cells led to higher design porosity, which contributed to a relatively stiffer mechanical behavior across both density levels. For samples with a 30% relative density, no significant changes were observed in the Young's modulus of lattices upon increasing the unit cell, where 74 ± 18 kPa were measured for 27-unit cells and 92 ± 3 kPa for 125-unit cells. However, in the case of lattices with a 40% relative density, stiffer structures were obtained by increasing the unit cell counts. Mean Young's modulus values of 167 ± 24 kPa, 185 ± 10 kPa, and 210 ± 10 kPa were obtained for lattices with 27-, 64-, and 125-unit cells, respectively. The Young's modulus values were extracted from the corresponding compressive stress–strain curves shown in Figure S3.

The influence of the unit cell counts on sensor sensitivity is illustrated in Figure 3c,d for 30% and 40% relative densities, respectively. The sensitivity values were calculated from the conductivity-vs.-compressive-stress plot shown in Figure S4. For lattices with 30% relative density, those containing 27- and 64-unit cells demonstrated comparable sensitivities of 4.91 ± 2.2 and 4.41 ± 0.84 kPa^{-1}, respectively, within the initial sensitivity region. However, the lattice with 125-unit cells showed a reduced mean sensitivity value of 3.26 ± 1.29 kPa^{-1}. This reduction in sensitivity can be attributed to the increased number of unit cells within a fixed area, which distributes the applied stress more uniformly. Consequently, each individual cell experiences less localized deformation, resulting in smaller changes in electrical current. This leads to a more uniform and smoother electrical response under compression. However, this similar trend was not observed for the 40% relative density lattices, where all samples showed similar mean sensitivity values in the initial region. In the wide pressure range, the sensitivity values remained relatively consistent across all samples, regardless of the unit cell count. These findings suggest that lattice structures with a 40% relative density offer the highest sensitivity and broader detection capability.

We selected 40% relative density and 64-unit cells as the parameters that yield the best balance between mechanical stiffness and electromechanical performance, and applied this design to fabricate lattice structures with Schwarz D and Gyroid geometries (Figure 4a). Their electromechanical properties were evaluated and compared to assess the influence of lattice topology on sensor

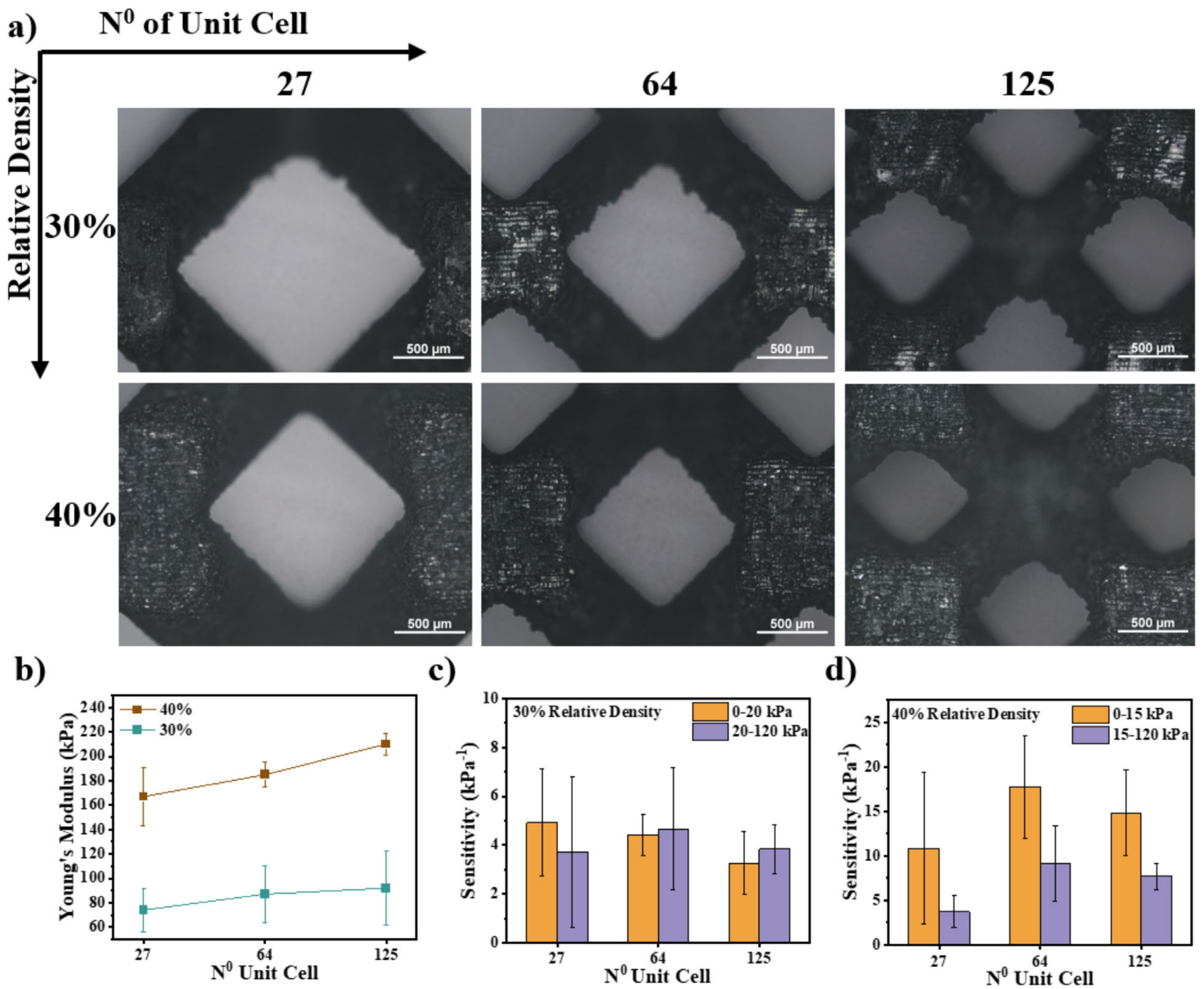

FIGURE 3 | (a) Microscopic pictures of the 3D Printed X-Cell lattices with 27, 64, and 125-unit cells, respectively, with 30% and 40% relative densities. (b) Mean Young's modulus of different lattices. Sensitivities of the lattices on different pressure ranges with (c) 30% and (d) 40% relative densities.

performance. Figure 4b presents the compressive stress–strain curves of the three lattice geometries. Each structure exhibited distinct stiffness characteristics across different strain ranges. Both the X-cell and Schwarz D lattices displayed an initial linear compression phase, followed by a reduction in displacement. The X-cell lattice began to show a decrease in displacement around 60 kPa, whereas the Schwarz D lattice maintained linearity until approximately 80 kPa, indicating a more deformable structure. In contrast, the Gyroid lattice exhibited a stiffer response up to 80 kPa, after which it underwent significant compression, reaching up to 50% strain. Figure 4c illustrates the sensitivity values of the different geometries. The sensitivity values were calculated from the conductivity-vs.-compressive-stress plot shown in Figure S5. The Gyroid-based structure demonstrated the highest performance, with a mean sensitivity of 40.03 ± 0.64 kPa^{-1} in the initial pressure range. In comparison, the X-cell and Schwarz D lattices exhibited lower sensitivities of 17.7 ± 5.8 and 7.4 ± 0.7 kPa^{-1}, respectively. Among the three geometries, the X-cell exhibited the highest sensitivity over the wide pressure range, achieving 9.11 ± 4.19 kPa^{-1}. In contrast, the Gyroid and Schwarz D structures showed more saturated responses, with sensitivities of 1.63 ± 1.16 and 2.06 ± 1.32 kPa^{-1}, respectively, across the wide pressure range. The obtained sensitivities and their corresponding pressure ranges are collected in Table 1.

The enhanced initial sensitivity of the gyroid lattice over other designs can be mainly attributed to its continuous surface topology, which provides a high density of parallel conductive pathways [48, 49]. The relatively thicker structural features may further promote conductive contact evolution under compression, contributing to stronger current modulation. In the wide pressure range, the gyroid lattice is getting more compact, leading to sensitivity saturation [37, 50]. The comparably higher sensitivities of the X-cell lattice across multiple zones make it an attractive option for pressure-sensor applications that require a linear, multi-zone sensing response [19, 51]. To evaluate the sensor's response characteristics, step-wise dynamic electromechanical responses of the lattice structures were evaluated by sequential pressure levels of 2, 5, and 10 kPa, as shown in Figure 4d. Each pressure level was maintained for 5 s to assess the sensor's responsiveness and stability. The current response curves for the three geometries corresponded closely to their respective initial sensitivities. The Gyroid structure exhibited the most pronounced current increase, beginning from pressures as low as 2 kPa. In contrast, the X-cell and Schwarz D lattices showed comparable

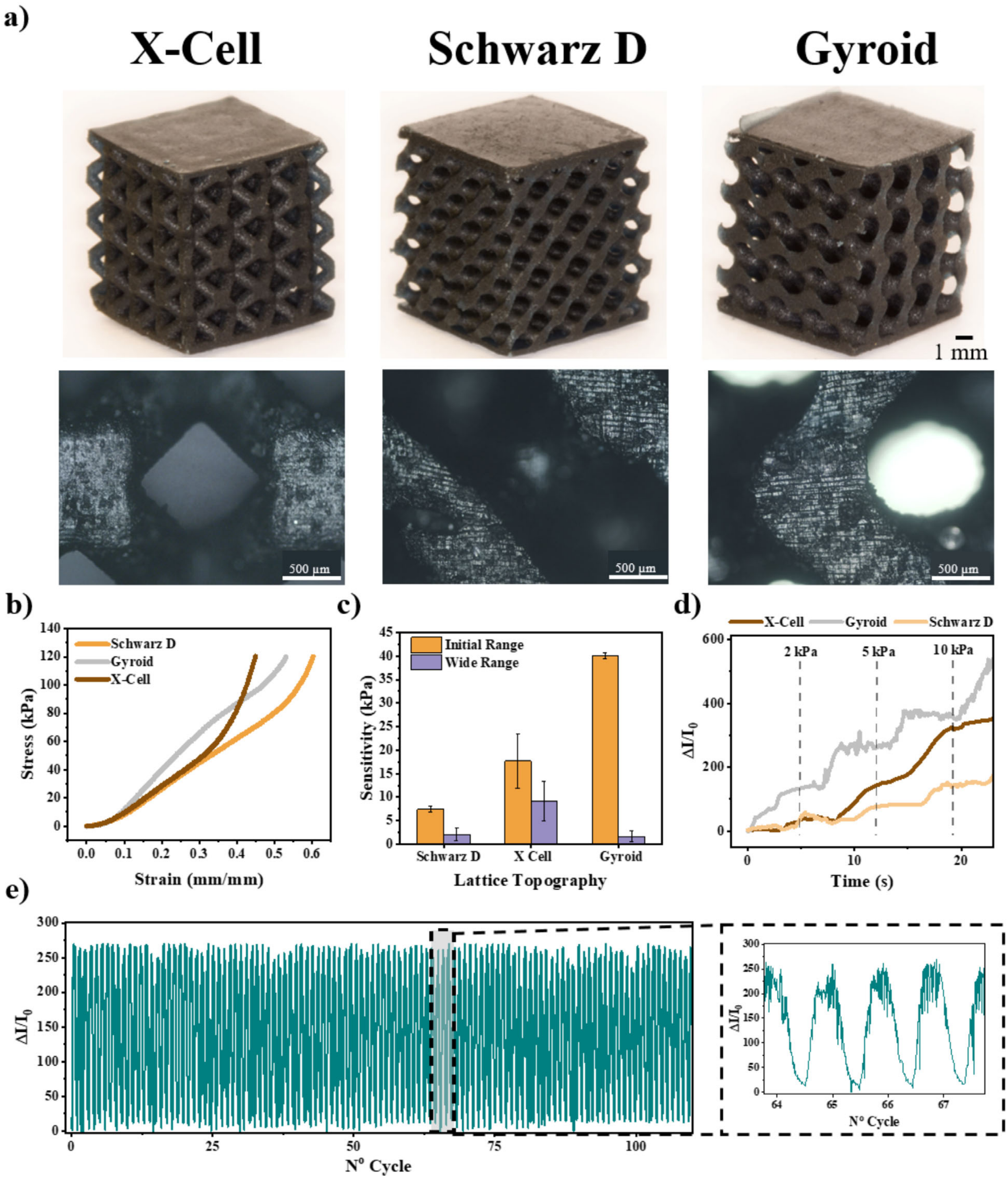

FIGURE 4 | (a) Pictures and corresponding microscope images of the 3D Printed X-Cell, Schwarz D, and Gyroid shaped lattices with 40% relative density and 64 Unit Cells, respectively. (b) Compressive stress-strain curves of different 3D printed lattices. (c) Mean sensitivities of the lattices at different sensitivity regions. (d) Step-like current change responses of lattices under the application of subsequent stress levels. (e) Cyclic stability of the Gyroid lattice structure under repeated loading between 0–5 kPa.

current outputs at 2 kPa. However, beyond 5 kPa, the X-cell structure demonstrated a distinct electromechanical response, diverging from the behavior observed in the Schwarz D geometry. This behavior not only corroborates the initial sensitivity values reported in Figure 4c, but also provides further insight into the responsiveness of the lattice structures under applied pressure. The Gyroid geometry exhibited the steepest slope in the current response, indicating the fastest reaction to incremental stress changes, likely due to its stiffer structure at that stress level. Overall, all three lattice geometries demonstrated distinct sensitivities and dynamic behaviors within the low-pressure range of 0–10 kPa, underscoring their potential for integration into

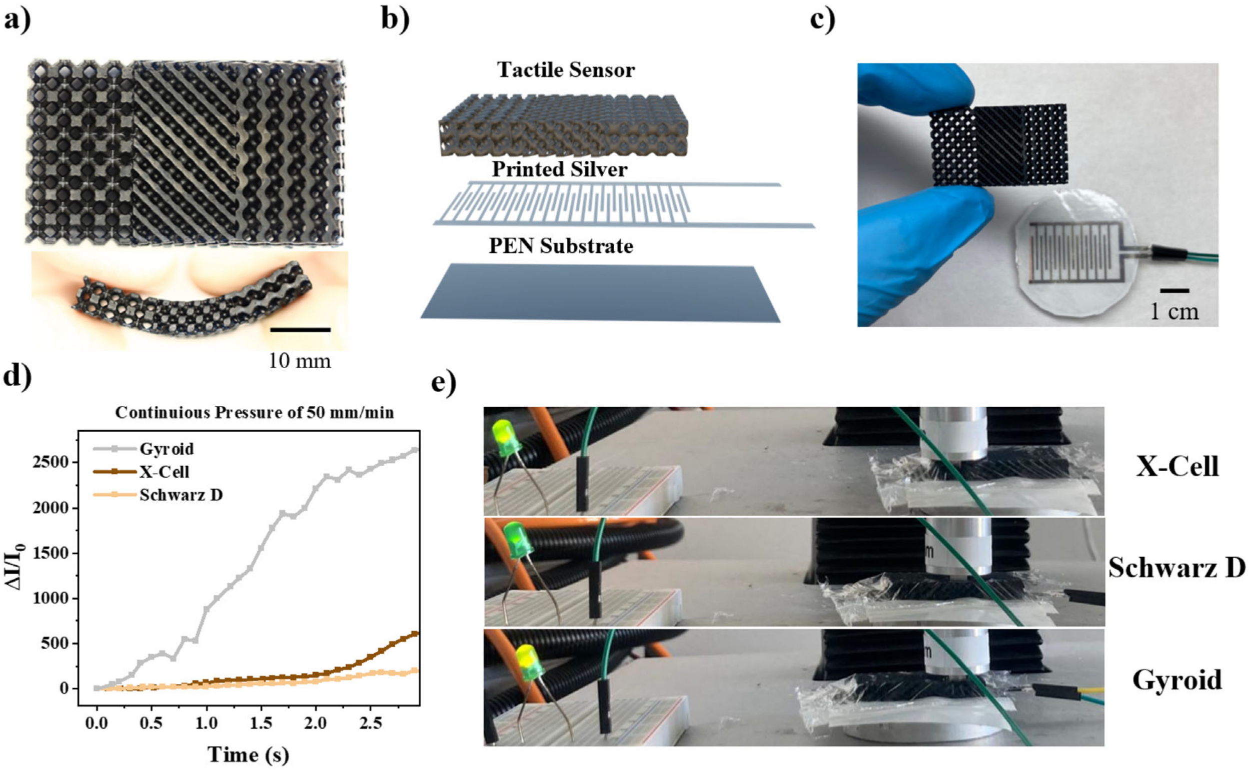

FIGURE 5 | (a) Pictures of the 3D printed pressure map combining X-Cell, Schwarz D, and Gyroid shaped lattices, respectively, with 40% relative density and 64 Unit Cells (b) Schematic representation of the electrode layout of the pressure map. (c) Picture of the pressure map sensor. (d) The electromechanical behavior between the different lattices. (e) Pictures of the LED intensity when using different-shaped lattices.

various real-time pressure sensing applications. Cyclic stability measurements of the gyroid lattice were performed between 0 and 5 kPa (Figure 4e). The device maintained a stable electrical response over 100 loading cycles, showing $\Delta I/I_0$ values from 0 to 250. This consistent cyclic behavior highlights its suitability for flexible pressure-sensor applications and indicates that the conductive network remains intact under repeated deformation.

2.3 | Proof of Concept Tactile Sensor Applications

To demonstrate practical applicability, a proof-of-concept tactile sensor was developed by leveraging the distinct electromechanical responses of the three lattice topologies into a single active layer, as shown in Figure 5a. This active sensing layer, with dimensions of 5 × 2.7 × 6 mm, was composed of three segments corresponding to the X-cell, Gyroid, and Schwarz D lattices. The composite layer was then integrated onto inkjet-printed interdigitated silver electrodes deposited on a flexible PEN (polyethylene naphthalate) substrate (Figure 5b,c).

The printed tactile sensor was encapsulated with stretch film to keep the sensor flat on the table and prevent bending during operation. Each lattice segment was electromechanically characterized under a compressive load of 50 mm min^{-1} (Figure 5d). The Gyroid structure exhibited the highest current variation response, followed by the X-cell and Schwarz D (Figure 5d), consistent with prior single-cell tests. The distinct electrical behavior of the sensor segments demonstrates that pressure localization can be achieved with a simple two-electrode measurement. The fabricated pressure sensor was incorporated into a simple circuit consisting of a battery and an LED, as illustrated in Figure 5e. When 50 kPa of stress was applied to each segment of the sensor to simulate the human touch, the LED brightness varied depending on its electromechanical properties. The brightest illumination occurred when pressure was applied to the gyroid section, followed by the X-cell, and then the Schwarz D lattice. The light intensity, as well as the measured current, can then be utilized to locate the position of applied pressure. These findings highlight the potential of using multi-lattice tactile sensors for spatial pressure mapping without the need for complex electrode array systems. By incorporating a broader range of lattice geometries with unique mechanical or dynamic response profiles, future systems could be trained to identify both the location and magnitude of applied forces, enabling advanced tactile sensing in robotics and wearable devices.

3 | Conclusions

In this study, a PEDOT:PSS-based acrylic photoresin was utilized to fabricate 3D lattice-oriented pressure sensors by digital light processing (DLP) in a single step, achieving feature sizes as small as 40 µm and eliminating the need for post-processing steps. The design of the 3D-printed conductive sensor was optimized by examining lattice characteristics such as relative density, unit cell configuration, and geometry. An X-cell-based lattice structure comprising 64-unit cells was used as the initial design to compare the effect of relative densities, ranging from 20% to 40%. All lattice structures demonstrated sensing activity across two distinct linear pressure regions between 0 and 120 kPa. The increase of the relative density had a pronounced effect on sensitivity, with approximately a five-fold enhancement for every 10% increase in relative density. In particular, the lattice with 40% relative density exhibited the highest sensitivity, reaching 17.7 ± 5.8 kPa^{-1} in the initial pressure range and 9.11 ± 4.19 kPa^{-1} in the wider range. Further analysis of unit cell count (27, 64, and 125) at constant density revealed minimal impact on sensitivity, despite a slight increase in stiffness. Finally, lattice structures with different orientations—Gyroid and Schwarz D—were 3D-printed and evaluated. The Gyroid cell exhibited the highest initial sensitivity, 40.03 ± 0.64 kPa^{-1}, in the range between 0–10 kPa. Reported 3D printed conductive lattice pressure sensors typically operate in the tens to hundreds of kPa regime, depending on topology, relative density, and conductive network design. 3D printed conductive lattice structures are working in a pressure range of 100 kPa regime. Therefore, each lattice geometry exhibited distinct sensitivity levels and response times. A proof-of-concept pressure mapping system was developed by integrating all three lattice geometries into a single platform. Each lattice exhibited distinct current transients over time, enabling pressure localization without the need for complex electrode systems. Overall, this work demonstrates a direct and efficient route for fabricating customizable conductive soft sensors and introduces a simplified design strategy for tactile sensing. Our single-step DLP method enables precise architectures that are difficult to achieve with conventional additive manufacturing techniques. This design strategy simplifies the electrode layout and supports scalable soft sensing technologies for applications such as soft grippers, electronic switches, and electronic skins, where adaptable and spatially resolved sensing is essential.

4 | Experimental Section

4.1 | Materials

PEDOT:PSS (Clevios PH 1000) was purchased from Heraeus. Ceramic 3DResyn CDP-WS water soluble and Fine Turner FT2 ultrafast photoinitiator were purchased from 3Dresyns. Poly(ethylene glycol) diacrylate (PEGDA, Mn = 700), ethylene glycol (EG), and silver nanoparticular ink (Silverjet) were purchased from Sigma–Aldrich.

4.2 | Photoresin Formulation

PEDOT:PSS conductive aqueous solution (50 wt.%) was mixed with Ceramic 3DResyn acrylate (34 wt.%) in a round-bottom flask. Subsequently, PEGDA crosslinker (8 wt.%), photoinitiator (4 wt.%), and EG additive (4 wt.%) were added to the mixture. The flask was protected from light exposure with aluminum foil and left stirring for 2 days to obtain a homogeneous mixture.

4.3 | Design of the 3D Printed Structures

Computer-Aided Design (CAD) models of all lattice structures were created in Fusion 360. For the X-Cell design, three relative-density configurations (20%, 30%, and 40%) were generated by varying the strut thicknesses to 400, 600, and 800 µm, respectively.

Lattices containing 27, 64, and 125-unit cells possess unit-cell sizes of 3.3, 2.5, and 2.0 mm, respectively. For the 30% relative-density condition, these lattices were fabricated with strut thicknesses of 800, 600, and 440 µm, while the 40% relative-density variants used strut thicknesses of 1100, 800, and 600 µm, respectively.

Additionally, X-Cell, Schwarz-D, and Gyroid lattices with 40% relative density and 64 unit cells were produced with strut thicknesses of 800, 700, and 1000 µm, respectively. Due to printing and post-processing effects, small deviations from nominal dimensions may occur.

4.4 | 3D Printing of the Conductive Photoresin and Silver Electrodes

The photoresin was loaded into the resin tank of the DLP printer (Asiga Max X27) and printed at 385 nm wavelength with a light intensity of 10.5 mW cm^{-2}. The optimal exposure times were 20 s for the burn-in layer and 2 s for the subsequent layers. The lattice architecture structures were manufactured with a 50 µm slice thickness. Then, the 3D printed conductive structures were washed with isopropyl alcohol (IPA) in an ultrasonic bath for 3 min, and the excess of IPA was blown away with a nitrogen gun. The resulting structures were further dried at RT for 15 min in a spinning plate and post-cured at λ: 405 nm for 1 min (Original Prusa Complete CW1).

The silver electrodes were inkjet-printed using an Ag nanoparticle ink on a PEN substrate using a Dimatix printer (DMP 2831) at a resolution of 725 dpi with a Dimatix Materials Cartridge Samba printhead by Fujifilm. The PEN substrate was treated with Ar plasma (Diener NANO Plasma Cleaner) at a flow rate of 65 mL min^{-1} for 20 s at a pressure of 0.35 mbar. Electrodes were crimped (CrimpFlex, Nicomatic SA) with contacts to form connections with the sensor.

4.5 | Characterization of the 3D Printed Structures

Electromechanical measurements were conducted by compressing the samples using an Alluris Universal Test Instrument FMT-310BU, with a 50 N load cell and displacement transducer head (FMT-310FUC5), and measuring the electrical resistance (at a source potential of 50 mV) with a Keithley 2612B source measurement unit. Micrographs were taken using an optical microscope (Nikon Eclipse 80i).

Acknowledgements

O.K. acknowledges the Carl Zeiss Foundation for the financial support. This work was funded by the German Research Foundation (Deutsche Forschungsgemeinschaft, DFG) under Germany's Excellence Strategy–2082/2–390761711. G.H.S. thanks DFG (Heisenbergprofessur, HE 7056/7-1) for the financial support. N.L.-L. gratefully acknowledges the support from the Spanish Ministry of Universities (FPU20/03416). M.C.-G. thanks

"Grant RYC2022-036380-I funded by MICIU/AEI /10.13039/501100011033 and FSE+," and the Emakiker program of POLYMAT (UPV/EHU). M.R.I. thanks the support of the "Programa de Perfeccionamiento de Personal Investigador Doctor, Gobierno Vasco" under Grant POS_2022_1_0050. K.C. receives financial support from the Karlsruhe Nano Micro Facility (KNMFi), a Helmholtz research infrastructure at the Karlsruhe Institute of Technology (KIT), and as part of the Helmholtz research programme MSE (Materials Systems Engineering) at KIT.

Open access funding enabled and organized by Projekt DEAL.

Conflicts of Interest

The authors declare no conflicts of interest.

Data Availability Statement

The data that support the findings of this study is available from the corresponding author upon request.

References

1. S. K. Dhinesh and K. L. Senthil Kumar, "A Review on 3D Printed Sensors," *IOP Conference Series: Materials Science and Engineering* 764 (2020): 012055, https://doi.org/10.1088/1757-899X/764/1/012055.

2. K. Cao, M. Wu, J. Bai, et al., "Beyond Skin Pressure Sensing: 3D Printed Laminated Graphene Pressure Sensing Material Combines Extremely Low Detection Limits With Wide Detection Range," *Advanced Functional Materials* 32 (2022): 2202360, https://doi.org/10.1002/adfm.202202360.

3. J. Kim, M. Lee, H. J. Shim, et al., "Stretchable Silicon Nanoribbon Electronics for Skin Prosthesis," *Nature Communications* 5 (2014): 5747, https://doi.org/10.1038/ncomms6747.

4. H. Moeinnia, D. J. Agron, C. Ganzert, L. Schubert, and W. S. Kim, "Wireless Pressure Monitoring System Utilizing a 3D-Printed Origami Pressure Sensor Array," *npj Flexible Electronics* 8 (2024): 21, https://doi.org/10.1038/s41528-024-00309-z.

5. M. E. Imanian, M. Kardan-Halvaei, F. Nasrollahi, A. Imanian, H. Montazerian, and V. Nasrollahi, "3D Printed Flexible Wearable Sensors Based on Triply Periodic Minimal Surface Structures for Biomonitoring Applications," *Smart Materials and Structures* 32 (2023): 015015, https://doi.org/10.1088/1361-665X/aca6bc.

6. S. Gong, W. Schwalb, Y. Wang, et al., "A Wearable and Highly Sensitive Pressure Sensor With Ultrathin Gold Nanowires," *Nature Communications* 5 (2014): 3132, https://doi.org/10.1038/ncomms4132.

7. W. Zhong, Q. Liu, Y. Wu, et al., "A Nanofiber Based Artificial Electronic Skin With High Pressure Sensitivity and 3D Conformability," *Nanoscale* 8 (2016): 12105–12112, https://doi.org/10.1039/C6NR02678H.

8. J. Park, Y. Lee, J. Hong, et al., "Giant Tunneling Piezoresistance of Composite Elastomers With Interlocked Microdome Arrays for Ultrasensitive and Multimodal Electronic Skins," *ACS Nano* 8 (2014): 4689–4697, https://doi.org/10.1021/nn500441k.

9. Y. Ma, Y. Yue, H. Zhang, et al., "3D Synergistical MXene/Reduced Graphene Oxide Aerogel for a Piezoresistive Sensor," *ACS Nano* 12 (2018): 3209–3216, https://doi.org/10.1021/acsnano.7b06909.

10. Q.-T. Lai, Q.-J. Sun, Z. Tang, X.-G. Tang, and X.-H. Zhao, "Conjugated Polymer-Based Nanocomposites for Pressure Sensors," *Molecules* 28 (2023): 1627, https://doi.org/10.3390/molecules28041627.

11. T. Xia, R. Yu, J. Yuan, et al., "Ultrahigh Sensitivity Flexible Pressure Sensors Based on 3D-Printed Hollow Microstructures for Electronic Skins," *Advanced Materials Technologies* 6 (2021), 2000984, https://doi.org/10.1002/admt.202000984.

12. G. L. Goh, W. Y. Yeong, J. Altherr, J. Tan, and D. Campolo, "3D Printing of Soft Sensors for Soft Gripper Applications," *Materials Today: Proceedings* 70 (2022): 224, https://doi.org/10.1016/j.matpr.2022.09.025.

13. W. Zhao, Z. Wang, J. Zhang, et al., "Vat Photopolymerization 3D Printing of Advanced Soft Sensors and Actuators: From Architecture to Function," *Advanced Materials Technologies* 6 (2021), 2001218, https://doi.org/10.1002/admt.202001218.

14. B. Shih, C. Christianson, K. Gillespie, et al., "Design Considerations for 3D Printed, Soft, Multimaterial Resistive Sensors for Soft Robotics," *Frontiers in Robotics and AI* 6 (2019): 30, https://doi.org/10.3389/frobt.2019.00030.

15. S. Peng, Y. Li, L. Wu, et al., "3D Printing Mechanically Robust and Transparent Polyurethane Elastomers for Stretchable Electronic Sensors," *ACS Applied Materials & Interfaces* 12 (2020): 6479–6488, https://doi.org/10.1021/acsami.9b20631.

16. Y. Yang, X. Li, M. Chu, et al., "Electrically Assisted 3D Printing of Nacre-Inspired Structures With Self-Sensing Capability," *Science Advances* 5 (2019): aau9490, https://doi.org/10.1126/sciadv.aau9490.

17. M. Alsharari, B. Chen, and W. Shu, "Sacrificial 3D Printing of Highly Porous, Soft Pressure Sensors," *Advanced Electronic Materials* 8 (2022): 2100597, https://doi.org/10.1002/aelm.202100597.

18. Q. Jin, C. Wang, H. Wu, et al., "3D Printing of Capacitive Pressure Sensors With Tuned Wide Detection Range and High Sensitivity Inspired by Bio-Inspired Kapok Structures," *Macromolecular Rapid Communications* 45 (2024): 2300668, https://doi.org/10.1002/marc.202300668.

19. Y. M. Yin, H. Y. Li, J. Xu, et al., "Facile Fabrication of Flexible Pressure Sensor With Programmable Lattice Structure," *ACS Applied Materials & Interfaces* 13 (2021): 10388–10396, https://doi.org/10.1021/acsami.0c21407.

20. H. Zhao, J. E. Huddy, W. J. Scheideler, and Y. Li, "Rational Design of 3D-Printed Metastructure-Based Pressure Sensors," *Advanced Engineering Materials* 25 (2023): 2301056, https://doi.org/10.1002/adem.202301056.

21. P. Verma, J. Ubaid, K. M. Varadarajan, B. L. Wardle, and S. Kumar, "Synthesis and Characterization of Carbon Nanotube-Doped Thermoplastic Nanocomposites for the Additive Manufacturing of Self-Sensing Piezoresistive Materials," *ACS Applied Materials & Interfaces* 14 (2022): 8361–8372, https://doi.org/10.1021/acsami.1c20491.

22. E. Davoodi, H. Montazerian, R. Haghniaz, et al., "3D-Printed Ultra-Robust Surface-Doped Porous Silicone Sensors for Wearable Biomonitoring," *ACS Nano* 14 (2020): 1520–1532, https://doi.org/10.1021/acsnano.9b06283.

23. H. Nassar, G. Khandelwal, R. Chirila, et al., "Fully 3D Printed Piezoelectric Pressure Sensor for Dynamic Tactile Sensing," *Additive Manufacturing* 71 (2023): 103601, https://doi.org/10.1016/j.addma.2023.103601.

24. Y. Xiao, C. Hu, L. Yang, J. Wu, and J. Li, "Preparation of Graphene/Polydimethylsiloxane Flexible Resistive Pressure Sensors Based on Direct Ink Writing 3D Printing," *Sensors and Actuators A: Physical* 382 (2025): 116148, https://doi.org/10.1016/j.sna.2024.116148.

25. G. Zhu, H. Dai, Y. Yao, et al., "3D Printed Skin-Inspired Flexible Pressure Sensor With Gradient Porous Structure for Tunable High Sensitivity and Wide Linearity Range," *Advanced Materials Technologies* 7 (2022): 2101239, https://doi.org/10.1002/admt.202101239.

26. R. Tao, J. Shi, F. Granier, M. Moeini, A. Akbarzadeh, and D. Therriault, "Multi-Material Fused Filament Fabrication of Flexible 3D Piezoelectric Nanocomposite Lattices for Pressure Sensing and Energy Harvesting Applications," *Applied Materials Today* 29 (2022): 101596.

27. C. Massaroni, L. Vitali, D. L. Presti, S. Silvestri, and E. Schena, "Fully Additively 3D Manufactured Conductive Deformable Sensors for Pressure Sensing," *Advanced Intelligent Systems* 6 (2024): 2300901, https://doi.org/10.1002/aisy.202300901.

28. J. Liu, Y. Liu, C. Deng, et al., "3D Printing Nano-Architected Semiconductors Based on Versatile and Customizable Metal-Bound Composite Photoresins," *Advanced Materials Technologies* 7 (2022): 2101230, https://doi.org/10.1002/admt.202101230.

29. J. Nam and M. Kim, "Advances in Materials and Technologies for Digital Light Processing 3D Printing," *Nano Convergence* 11 (2024): 45, https://doi.org/10.1186/s40580-024-00452-3.

30. X. Xia, Z. Xiang, Z. Gao, et al., "Structural Design and DLP 3D Printing Preparation of High Strain Stable Flexible Pressure Sensors," *Advanced Science* 11 (2024): 2304409, https://doi.org/10.1002/advs.202304409.

31. T. Xiao, Y. Chen, Q. Li, Y. Gao, L. Pan, and F. Xuan, "All Digital Light Processing-3D Printing of Flexible Sensor," *Advanced Materials Technologies* 8 (2023), 2201376, https://doi.org/10.1002/admt.202201376.

32. X. Zhao, W. Wang, Z. Wang, et al., "Flexible PEDOT:PSS/Polyimide Aerogels With Linearly Responsive and Stable Properties for Piezoresistive Sensor Applications," *Chemical Engineering Journal* 395 (2020): 125115, https://doi.org/10.1016/j.cej.2020.125115.

33. Y. Ding, J. Yang, C. R. Tolle, and Z. Zhu, "Flexible and Compressible PEDOT:PSS@Melamine Conductive Sponge Prepared via One-Step Dip Coating as Piezoresistive Pressure Sensor for Human Motion Detection," *ACS Applied Materials & Interfaces* 10 (2018): 16077–16086, https://doi.org/10.1021/acsami.8b00457.

34. N. Lopez-Larrea, A. Gallastegui, L. Lezama, M. Criado-Gonzalez, N. Casado, and D. Mecerreyes, "Fast Visible-Light 3D Printing of Conductive PEDOT:PSS Hydrogels," *Macromolecular Rapid Communications* 45 (2024): 2300229, https://doi.org/10.1002/marc.202300229.

35. H. Abdullah and T. Phairatana, "A Study on the Performances of PEGDA and PEDOT: PSS Composite Resin for 3D-Printed Biosensor Applications," *ECS Transactions* 107 (2022): 15001–15010, https://doi.org/10.1149/10701.15001ecst.

36. N. Lopez-Larrea, M. Criado-Gonzalez, A. Dominguez-Alfaro, et al., "Digital Light 3D Printing of PEDOT-Based Photopolymerizable Inks for Biosensing," *ACS Applied Polymer Materials* 4 (2022): 6749–6759, https://doi.org/10.1021/acsapm.2c01170.

37. J. Fu, S. E. Taher, R. K. Abu Al-Rub, T. Zhang, V. Chan, and K. Liao, "Engineering 3D-Architected Gyroid MXene Scaffolds for Ultrasensitive Micromechanical Sensing," *Advanced Engineering Materials* 24 (2022): 2101388, https://doi.org/10.1002/adem.202101388.

38. H.-G. Kim, S. Hajra, H. Lee, N. Kim, and H. J. Kim, "Additively Manufactured Mechanical Metamaterial-Based Pressure Sensor With Tunable Sensing Properties for Stance and Motion Analysis," *Advanced Engineering Materials* 25 (2023): 2201499, https://doi.org/10.1002/adem.202201499.

39. Q. Guan, B. Dai, H. Sonar, and J. Hughes, "Inverse Co-Design of Mechanical and Sensory Properties in Soft Lattice Foams for Multifunctional Wearables," *Advanced Science* 12 (2025): 07102, https://doi.org/10.1002/advs.202507102.

40. M. Askari, D. A. Hutchins, P. J. Thomas, et al., "Additive Manufacturing of Metamaterials: A Review," *Additive Manufacturing* 36 (2020): 101562, https://doi.org/10.1016/j.addma.2020.101562.

41. J. Han, Z. Li, S. Kong, S. Tang, D. Feng, and B. Li, "Wide-Response-Range and High-Sensitivity Piezoresistive Sensors With Triple Periodic Minimal Surface (TPMS) Structures for Wearable Human-Computer Interaction Systems," *Composites Part B: Engineering* 287 (2024): 111840, https://doi.org/10.1016/j.compositesb.2024.111840.

42. M. S. Hossain, M. M. Hossain, and S. Nilufar, "An Overview of Additive Manufacturing of Triply Periodic Minimal Surface (TPMS) Structures," *Polymers* 17 (2025): 3307, https://doi.org/10.3390/polym17243307.

43. Z. Han, H. Li, J. Xiao, et al., "Ultralow-Cost, Highly Sensitive, and Flexible Pressure Sensors Based on Carbon Black and Airlaid Paper for Wearable Electronics," *ACS Applied Materials & Interfaces* 11 (2019): 33370–33379, https://doi.org/10.1021/acsami.9b12929.

44. X. Fu, L. Wang, L. Zhao, et al., "Controlled Assembly of MXene Nanosheets as an Electrode and Active Layer for High-Performance Electronic Skin," *Advanced Functional Materials* 31 (2021): 2010533, https://doi.org/10.1002/adfm.202010533.

45. G. Gilanizadehdizaj, D. Bhattacharyya, J. Stringer, and K. Aw, "Elucidating the Conducting Mechanisms in a Flexible Piezoresistive Pressure Sensor Using Reduced Graphene Oxide Film in Silicone Elastomer," *Sensors* 23 (2023): 2443, https://doi.org/10.3390/s23052443.

46. L. Gao, M. Wang, W. Wang, et al., "Highly Sensitive Pseudocapacitive Iontronic Pressure Sensor With Broad Sensing Range," *Nano-Micro Letters* 13 (2021): 140, https://doi.org/10.1007/s40820-021-00664-w.

47. T. Li, P. Pan, Z. Yang, et al., "3D Printing of a Flexible Inclined-Tip Cone Array-Based Pressure Sensor," *Advanced Materials Technologies* 7 (2022): 2101135, https://doi.org/10.1002/admt.202101135.

48. S. Kong, Z. Li, J. Han, et al., "High-Performance Flexible Piezoresistive Pressure Sensors With Composite Materials and 3D Lattice Structures for Advanced Health Monitoring," *Industrial & Engineering Chemistry Research* 64 (2025): 15658–15671, https://doi.org/10.1021/acs.iecr.5c01324.

49. M. S. El-Asfoury, N. E. El-Bedwehy, M. Shazly, and A. Elkaseer, "Orientation Driven Design and Mechanical Optimization of Gyroid TPMS Lattice Structures," *Scientific Reports* 16 (2026): 4373, https://doi.org/10.1038/s41598-026-35201-5.

50. S. Sharma, A. Chhetry, M. Sharifuzzaman, H. Yoon, and J. Y. Park, "Wearable Capacitive Pressure Sensor Based on MXene Composite Nanofibrous Scaffolds for Reliable Human Physiological Signal Acquisition," *ACS Applied Materials & Interfaces* 12 (2020): 22212–22224, https://doi.org/10.1021/acsami.0c05819.

51. J. E. Huddy, A. P. Tiwari, H. Zhao, Y. Li, and W. J. Scheideler, "Graph Theory Design of 3D Printed Conductive Lattice Electrodes," *Advanced Materials Technologies* 8 (2023): 2300180, https://doi.org/10.1002/admt.202300180.

Supporting Information

Additional supporting information can be found online in the Supporting Information section.

Supporting File: admt70896-sup-0001-SuppMat.docx.